Summer Student Report:

Finite Element Method Analysis of Dipole Beam Position Monitor Cable Distortion and PSB Quadrupole Lifting

by **Katrīna Rimša**

at the EN-MME-EDS unit

under the supervision of:
Federico Carra

September 27, 2024

Abstract

The aim of this report is to introduce the reader to the projects carried out during the 13-week studentship at the EN-MME-EDS unit. Two finite element analyses are discussed - High-Luminosity Large Hadron Collider dipole Beam Position Monitor cables distortion and Proton Synchrotron Booster quadrupole lifting.

The distortion of the Beam Position Monitor cables is a consequence of thermal contractions occurring within the cold mass. The results of the numerical analysis indicated that, when subjected to a displacement of 50 mm in the negative y-direction, five out of the eight cables exhibited a relatively high degree of plastic strain, with values exceeding 1%. However, more realistic load cases of 30 mm and 15 mm demonstrated acceptable plastic strains (less than 1%) and only elastic deformation, respectively. Therefore, no modifications to the design were deemed necessary.

The replacement of 48 quadrupole magnets within the Proton Synchrotron Booster has highlighted the importance of safe quadrupole handling. The simulation results portray that the current vertical lifting design is in compliance with the load lifting and steel joint standards. However, the bottom component for horizontal lifting must be redesigned to enhance the safety factors.

Acknowledgements

I wish to express my gratitude to the entire EN-MME group for welcoming me into their fold and for their willingness to assist, even when the questions were beyond the scope of their expertise. I would like to share immense appreciation to my supervisor **Federico Carra** for sharing his knowledge in a coherent manner and always bringing a positive attitude within the workplace. Additionally, without the help and guidance of **Carlotta Accettura**, **Audrey Piccini** and **Joanna Sylwia Swieszek** I wouldn't have achieved this level of Ansys proficiency so quickly. I would like to thank **Robin Betemps** for providing me with an opportunity to engage in a multidisciplinary project and for being approachable whenever necessary. Thanks to my practical work colleagues **Luisa Puddu** and **Laura Hannemann** for teaching me useful hands-on instrument skills. Last but not least, I am grateful to my peers **Alix Renata Marie Lemoine** and **Nicolas Andres Avellan Marin** for making the (short) breaks more frequent and rainy days feel sunnier with their continuous willingness to yappa yappa.

Contents

1 Dipole Beam Position Monitor cables distortion

1.1 Introduction

The Beam Position Monitor (BPM) system provides information on the positions of the propagating beams by determining the beam's centre of mass [1]. Four pick-up plates measure the time-dependent electric field of the beam particles. The voltages recorded by the BPM are transmitted via cable from the accelerator tunnel, where they are transformed into meaningful signals [2]. In the High-Luminosity Large Hadron Collider (HL-LHC) dipole vacuum chamber, 8 new BPM cables will be installed. One end is connected to the vacuum tank flange (positioned outside the cold mass) and the other end is attached to the BPM flange (situated inside the cold mass) as depicted in Figure 1. The cool-down of the mass generates a contraction at the cold end of the cable, which in turn imposes stresses and displacement throughout the cable. The behaviour was modelled using Ansys Workbench 2023 R2. Hence, two main objectives were determined:

1. Check for cable interactions in the system.
2. Verify the generated stress on each cable;
   (a) if exceeds the yield point, determine the plastic strain.

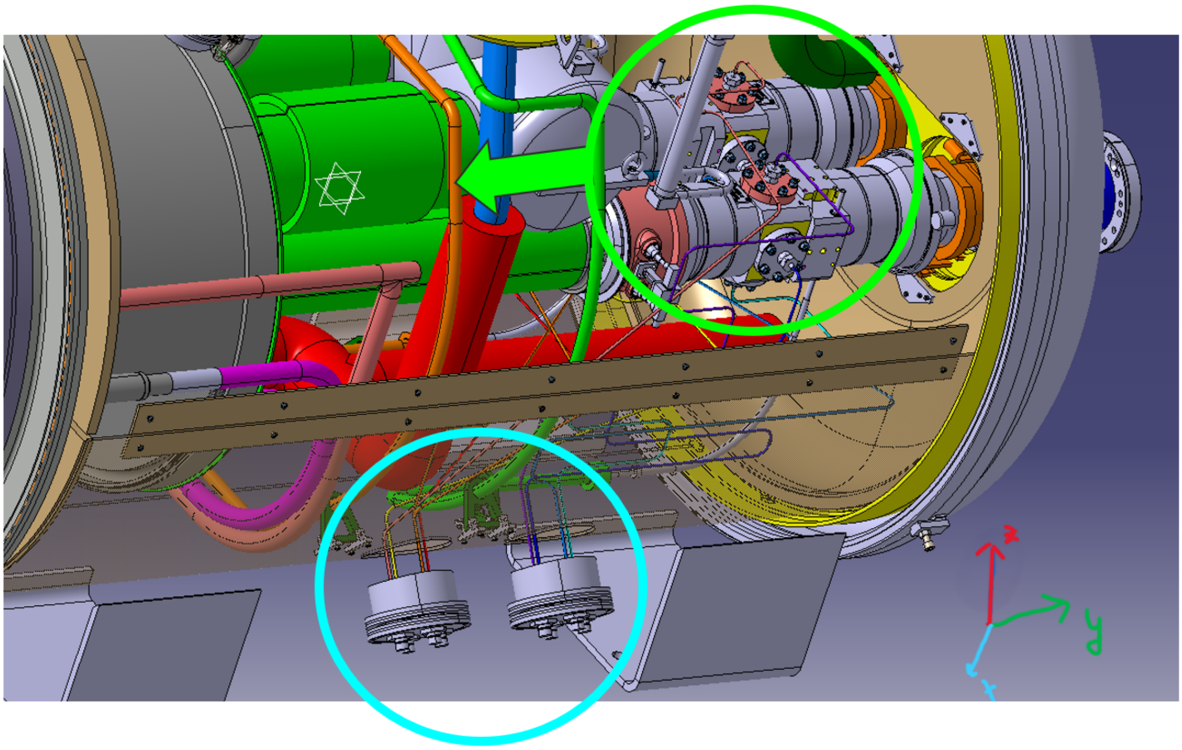

Figure 1: The displacement is imposed inside the cold mass (green) and position is fixed outside the cold mass (blue).

1.2 Methodology

1.2.1 Geometry

The eight cables' geometry was simplified based on several assumptions:

1. The BPM cable has a coaxial configuration with three parts - centre conductor, dielectric and outer conductor (Figure 2). The outer conductor accounts for 99% of the cable's structural stiffness, thus, the other parts can be neglected.

2. Cables can be modelled using shell elements.

3. Outer conductor is made out of SS-304L. Material properties are depicted in Table 1.

Property	Value
Poisson's Ratio	0.27 [3]
Yield Strength [MPa]	175 [4]
Young Modulus [GPa]	200 [5]
Elongation at fracture [%]	45 [6]
Density [g/m^3]	7.9 [7]

Table 1: SS-304L properties.

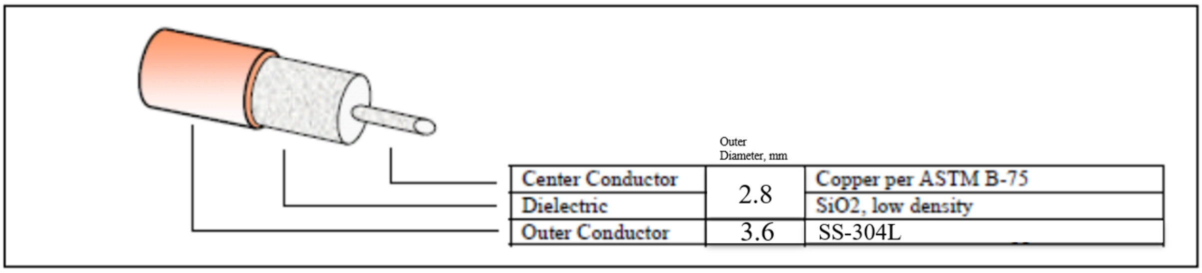

Figure 2: BPM cable configuration and materials.

Based on the aforementioned mechanical assumptions, the cable geometry was simplified as shown in Figure 3 and each cable was designed as depicted in Figure 4. The cables were assigned different colours to distinguish each cable more easily.

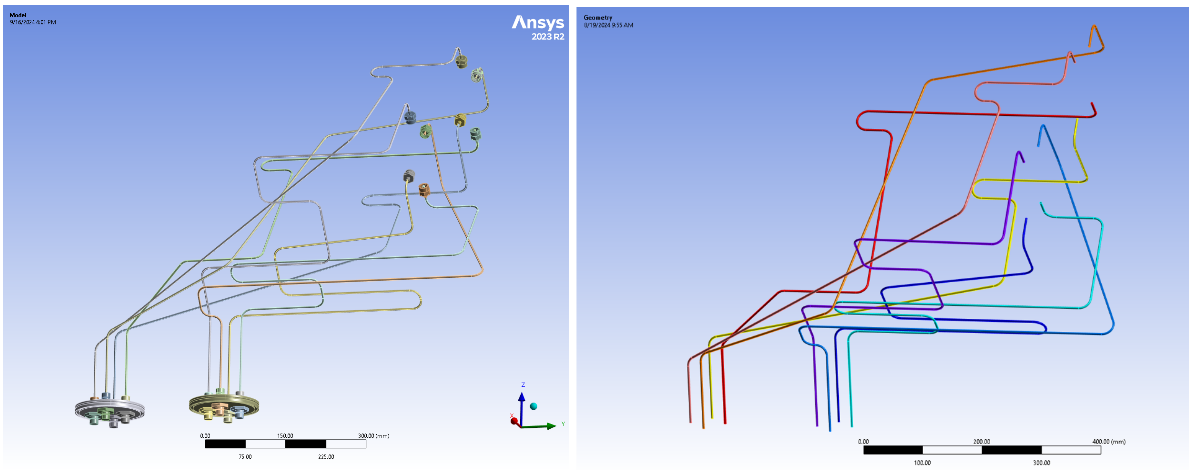

Figure 3: Original geometry (left) and simplified geometry (right).

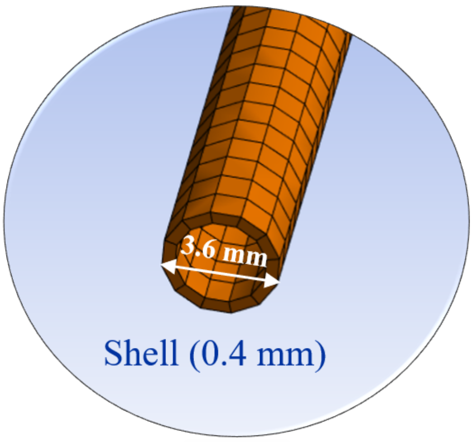

Figure 4: Shell geometry of the orange BPM cable.

1.2.2 Boundary and Load Condition

A new coordinate system was introduced to facilitate the load application with respect to the geometry. The coordinate system was rotated around y-axis to 45°. The imposed displacements depend on the load cases:

- load case 1: (0, -50, -3) mm;
- load case 2: (0, -30, -3) mm;
- load case 3: (0, -15, -3) mm;

at the BPM flanges and fixed support at the vacuum tank flanges for each cable (Figure 5). Standard earth gravity was also applied.

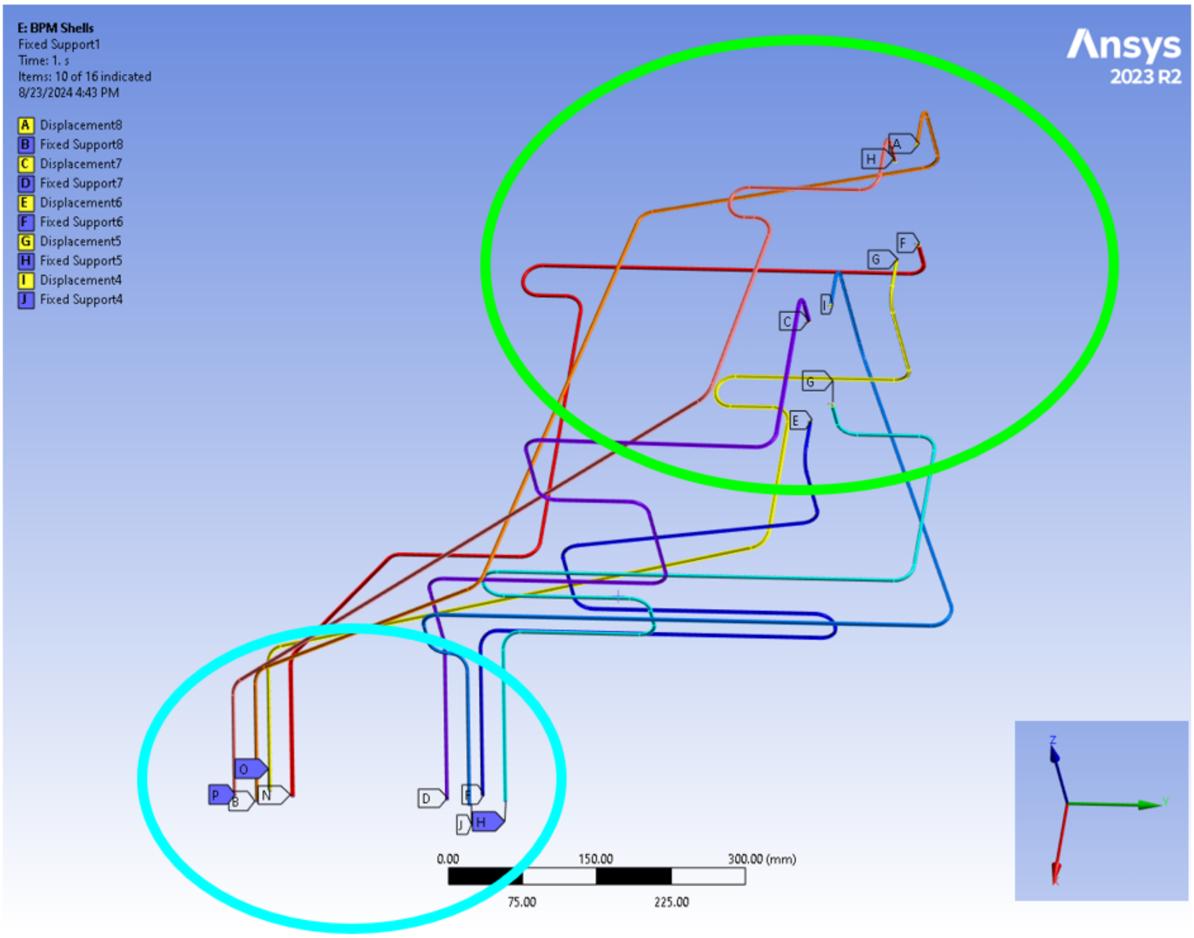

Figure 5: Applied displacement in the negative y-direction and z-direction (green) and fixed support (blue).

1.3 Results

1.3.1 Objective 1

Results of (0, -50, -3) mm displacement showcase a small compenetration between the turquoise and violet cable (Figure 6). However, this is not expected to add additional stress, as the components are very flexible and only making minimal mechanical interaction.

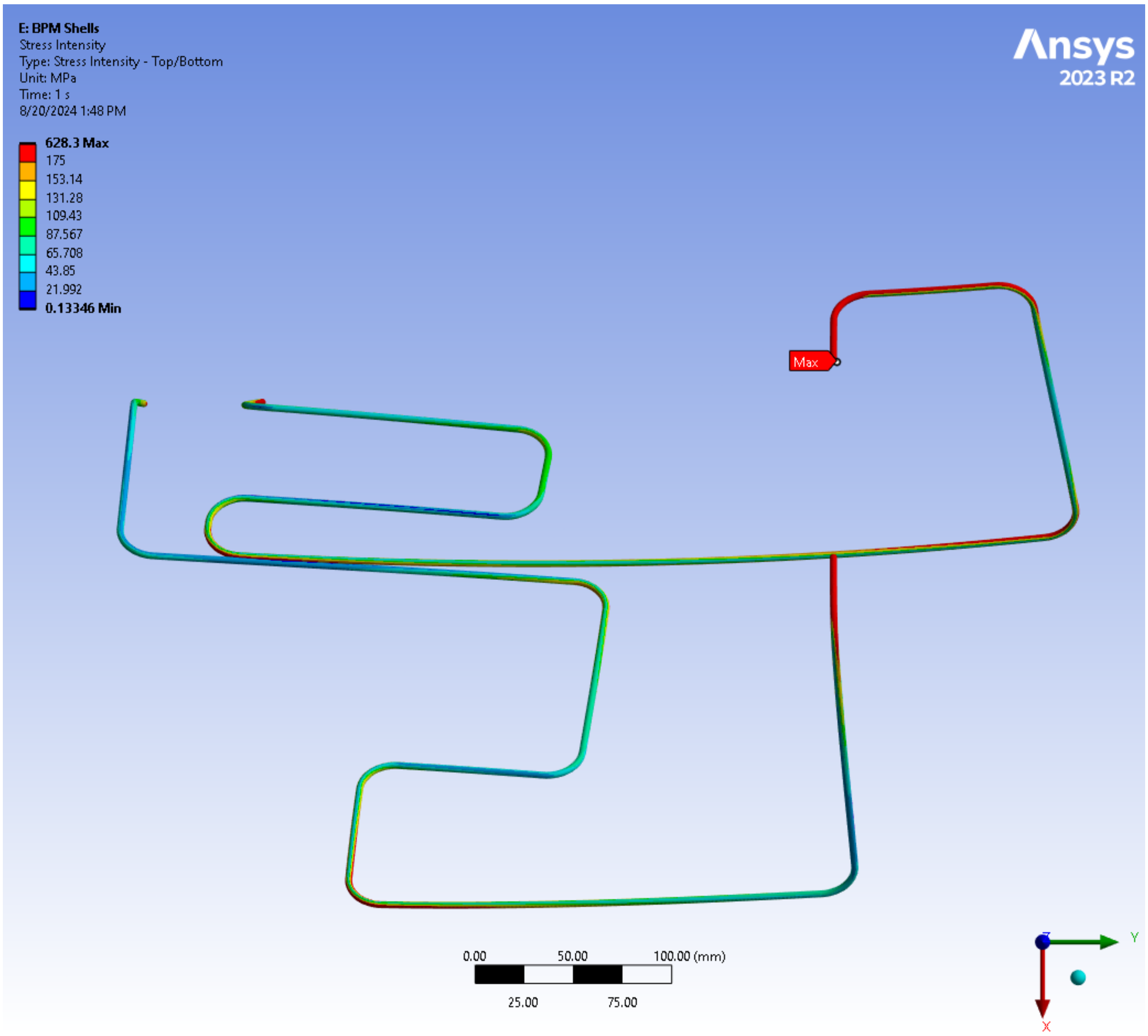

Figure 6: Contact between turquoise and violet cable after displacement.

1.3.2 Objective 2

The elastic model showed that yield point of 175 MPa (red regions) was exceeded for all cables in the fixed and displacement extremities or elbows (Figure 7). Thus, an elasto-plastic model was also investigated to determine the amount of plastic strain achieved (Figure 8).

Figure 7: Elastic model results.

Cable	Max. plastic strain, %		
	50 mm	30 mm	15 mm
PINK	**1,01**	0,06	0,00
YELLOW	**2,67**	0,11	0,00
RED	0,02	0,00	0,00
LIGHTBLUE	0,03	0,00	0,00
TURQUOISE	**1,72**	0,09	0,00
DARKBLUE	**2,17**	0,19	0,00
VIOLET	**1,03**	0,06	0,00
ORANGE	0,03	0,00	0,00

Legend

bold	strain > 1%
bold	strain > 1% at the fixed extremity

with 30 mm, max. plastic strain occurs at the ***displacement*** *extremity*

Figure 8: BPM maximum plastic strain results for 50 mm, 30 mm and 15 mm displacement in the negative y-direction.

1.4 Conclusion

A displacement of (0, -50, -3) mm was applied to 8 BPM cables to simulate thermal contraction within the dipole cold mass. The simulation results indicate minimal contact between the turquoise and violet cables. Additionally, all cables exceeded the yield point. With a 50 mm displacement, 5 out of 8 cables experienced plastic strain greater than 1% in localized regions. In one of these cables, the highest strain occurred at the fixed end, which remains at room temperature. More realistic displacement scenarios were also examined. With a 30 mm displacement, 5 cables exceeded the yield limit, but the plastic strain remained below 1%, which is acceptable. Lastly, with a 15 mm displacement, all cables stayed within the elastic range. In both cases, no contact between cables was observed. Since the results improved for the load cases 2 and 3, the cable geometry is acceptable and no design implications are necessary.

2 Proton Synchrotron Booster quadrupole lifting

2.1 Introduction

The Proton Synchrotron Booster (PSB) requires the replacement of 48 quadrupole magnets due to water leakage [8]. In the discussion how to produce new ones, the handling of the magnets is an important topic. The focusing quadrupole (QF) and defocusing quadrupole (QD) are lifted in two positions: vertical and horizontal (Figure 9). The handling systems must comply with the load lifting standard (EN 13155:2020) and the design of steel joints (EN 1993-1-8). The lifting standard requires additional 2G and 3G analysis, where no plastic strain can be accepted and plastic strain can be accepted with the condition that the load is not released, respectively [9][10]. Consequently, the objectives were to:

1. validate the existing vertical lifting design according to the standards;
2. design a bottom component for the horizontal lifting;
    (a) validate the horizontal lifting components according to the standards.

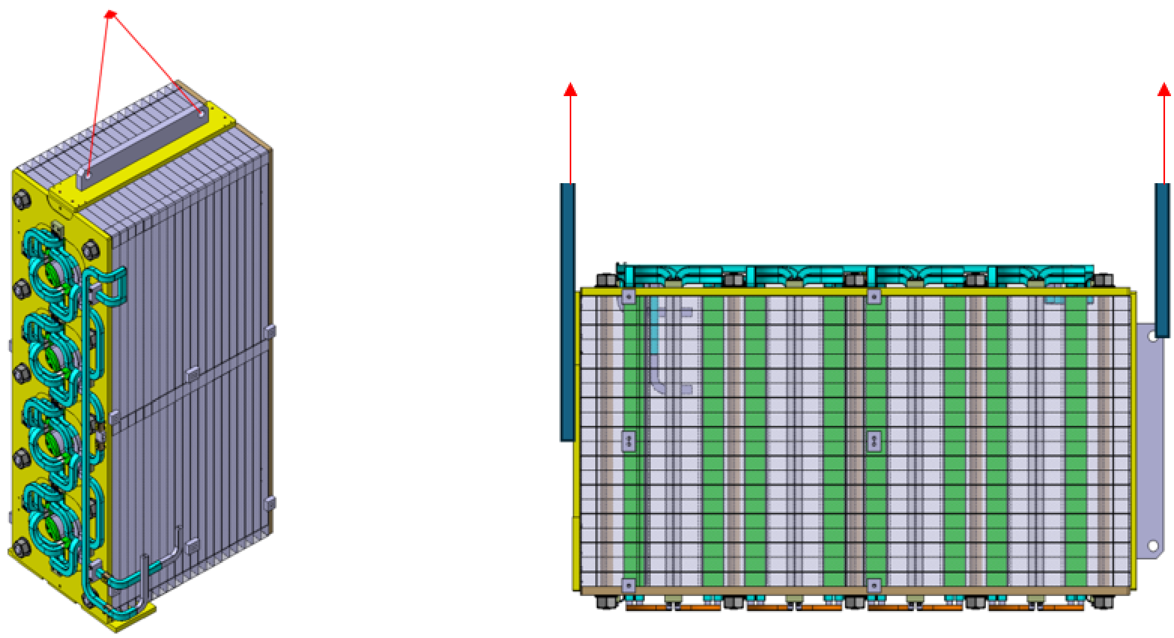

Figure 9: Defocusing quadrupole vertical lifting (left) and horizontal lifting (right) positions.

2.2 Methodology

2.2.1 Geometry

The geometry was simplified to focus on the essential lifting components, as the simulations do not require the full detail of the quadrupole structure (Figure 10). Only the relevant lifting and magnet elements, such as mass and dimensions, were kept to execute the analysis. Mass of QF and QD are 3 t and 5 t, respectively. The difference between QF and QD lifting components' dimensions is depicted in Figure 11.

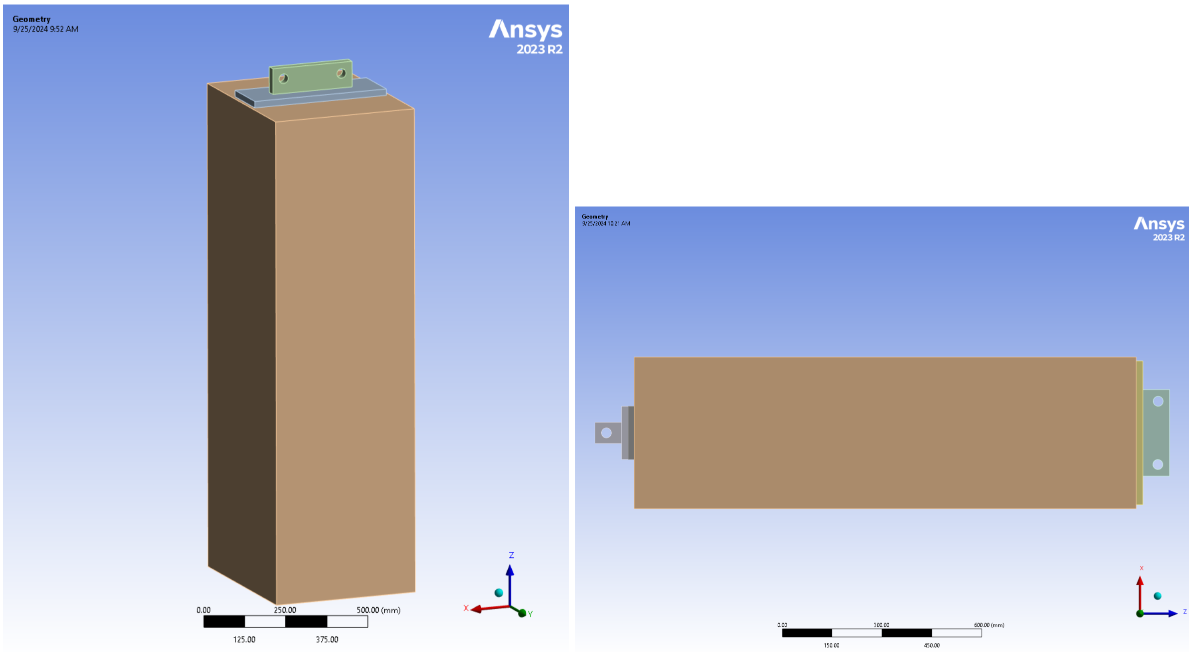

Figure 10: Simplified vertical QF geometry (left) and horizontal geometry (right).

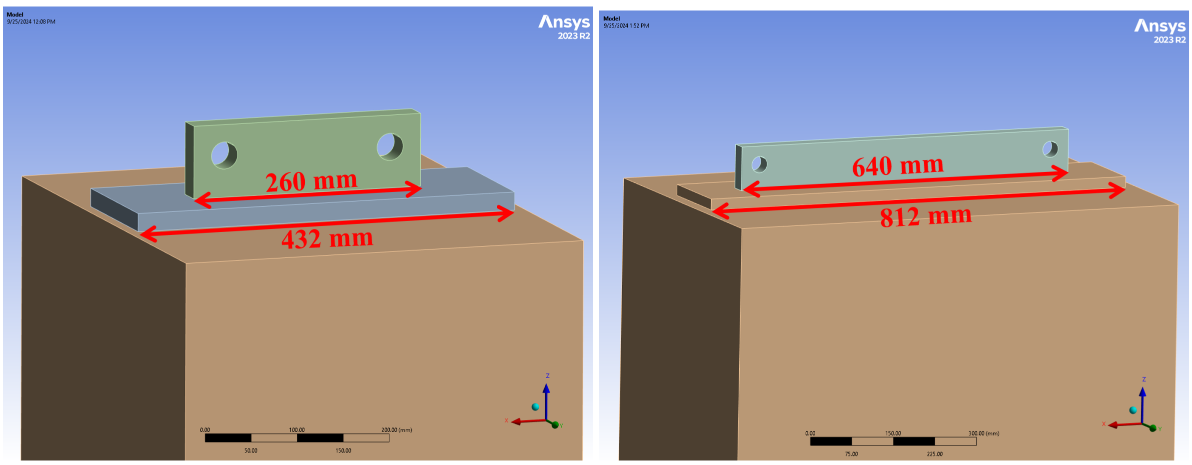

Figure 11: QF (left) and QD (right) lifting component dimensions. Heights and widths are equal between the components of the magnets.

For the horizontal lifting, an additional component was designed on the bottom of the QF magnet. This design was inspired by other existing lifting designs. The bottom plate was already an integrated part of the quadrupole magnets, secured by four M16 bolts in the centre. To complement this and facilitate the handling process, a top plate was designed with four M16 bolts matching with the bottom plate. The edges of the hang are welded to the inside walls of the top plate.

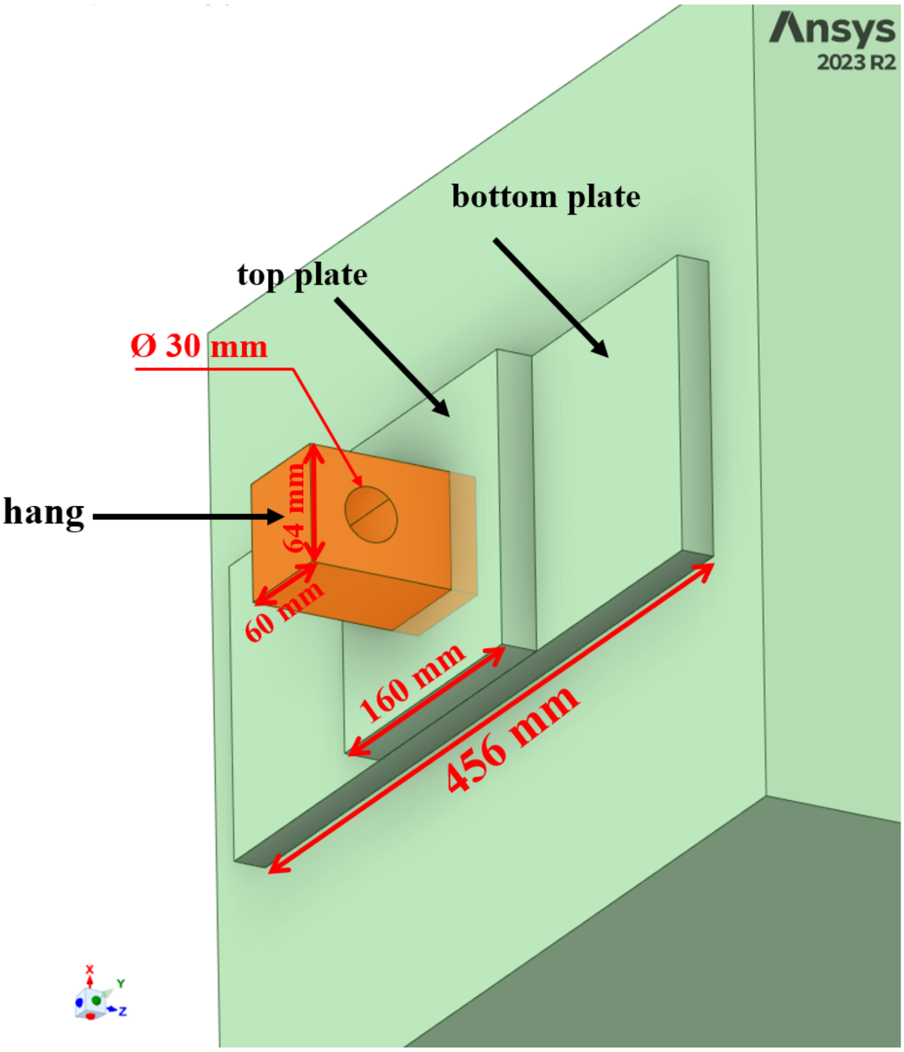

Figure 12: QF horizontal lifting left component design. Height of the hang is is 95 mm. Height of the top plate is 20 mm and bottom plate is 18 mm.

To verify the lifting components, their contact reaction forces were investigated. The contact was modelled by joining an edge with a face. For example, individual edges of the support block were joined to a magnet face and the vertical hang edges were connected to the support's top face from all sides (Figure 13). The weld size for connecting support and magnet is 5x5 mm and for joining the vertical hang and support, the size is 11x11 mm for each edge.

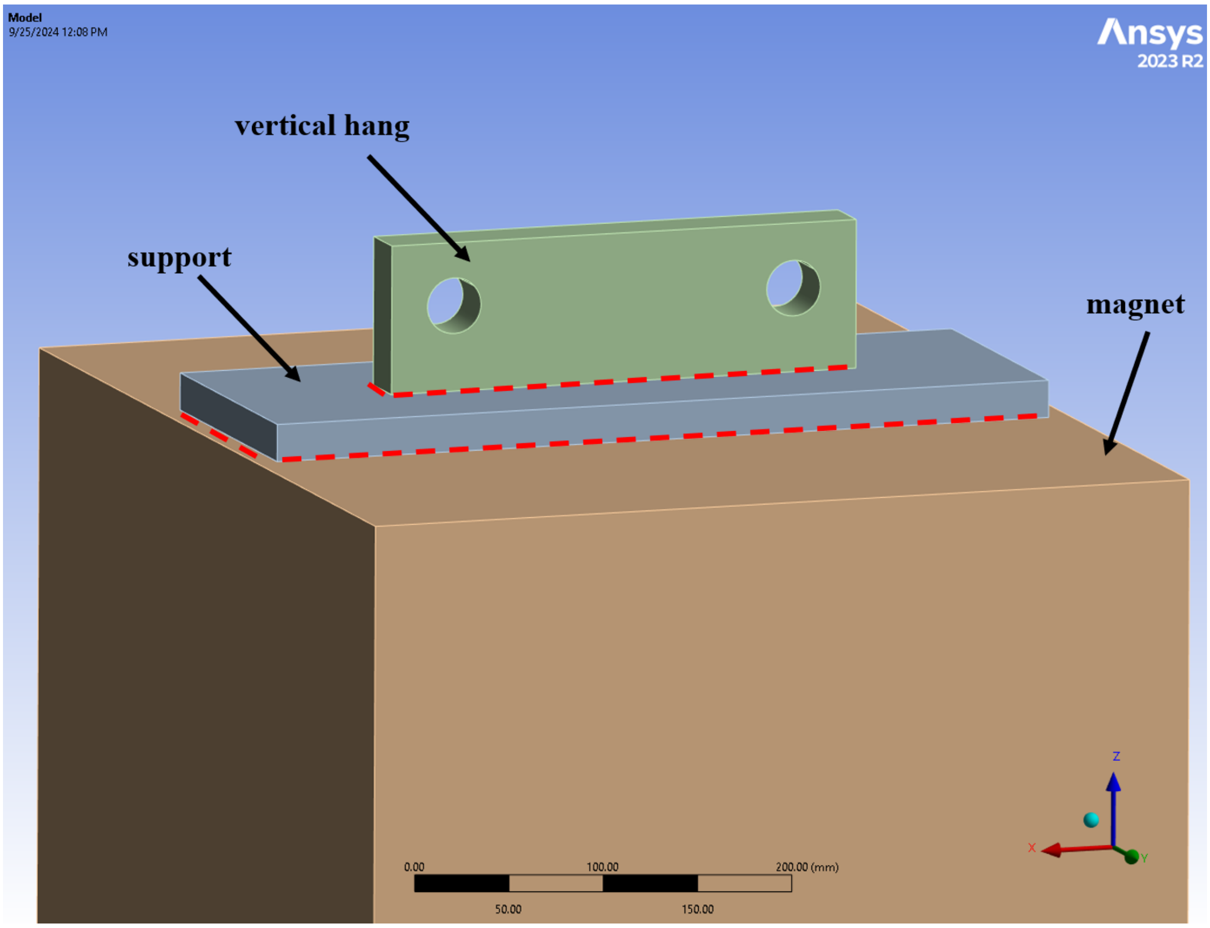

Figure 13: QF vertical lifting contact regions (red dashed lines).

In Figure 12, the all-around edge-to-face contacts were implemented for bottom plate and magnet and hang and top plate connections. However, the face-to-face contact was used for connecting the top and bottom plates to assess the bolt preload (discussed in section 2.3.2).

2.2.2 Boundary and Load Condition

Lifting behaviour was simulated using Ansys Workbench 2023 R2 software. For the vertical lifting, one remote point (500 mm in the positive z-direction) connected to the hanging element holes was used to initiate remote displacement (Figure 14). To verify the lifting standard, three load cases were investigated:

- Load case 1: acceleration in the positive z-direction of 9806 mm/s^2;
- Load case 2: acceleration in the positive z-direction of 19613 mm/s^2;
- Load case 3: acceleration in the positive z-direction of 29420 mm/s^2.

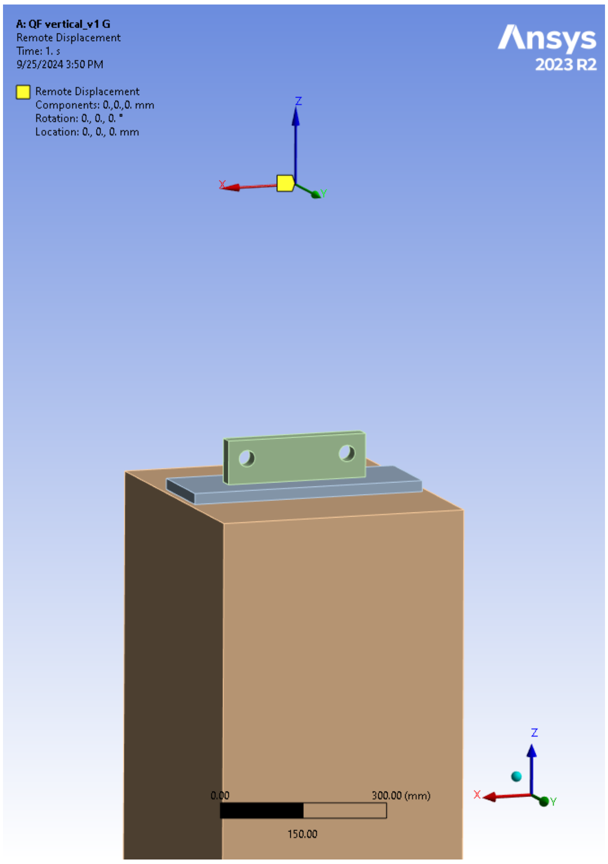

Figure 14: QF vertical boundary conditions (QD boundaries were identical).

For the horizontal lifting, the same load cases were applied. However, two separate remote points and displacements were used to simulate straight horizontal handling (Figure 15).

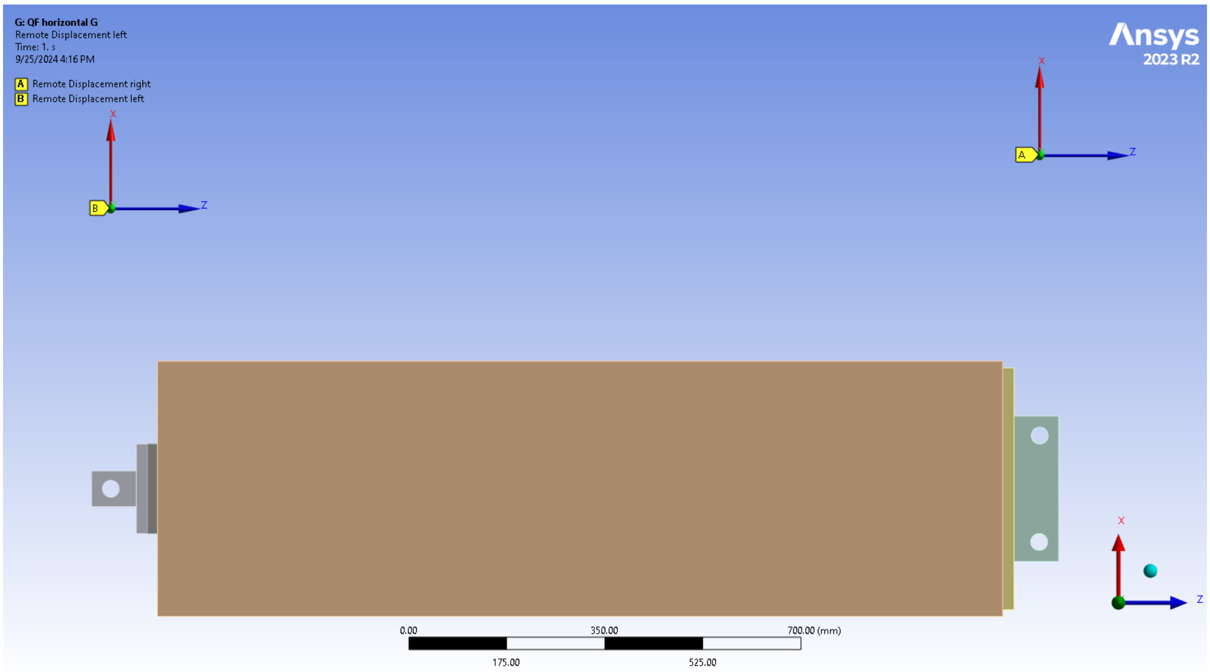

Figure 15: QF horizontal lifting boundary conditions.

2.3 Results

2.3.1 Vertical lifting

All load cases showed no plastic strain for both QF and QD magnets. Additionally, the weld utilisation factors were in the range from 1.9% to 19.8% for the QF magnet and from 1.8% to 26.8% for the QD magnet.

2.3.2 Horizontal lifting

Horizontal lifting results were done only for the QF magnet thus far. Load cases of G and 2G acceleration showed no plastic strain. However, a maximum plastic strain of 0.08% occurred with the 3G load case. The weld utilisation factor ranged from 0.4% to 59.4%, which is acceptable. However, the bolt assessment for G and 2G load cases showed a safety factor of 2 and 1, respectively. The unsatisfactory result comes mainly from the relatively large shear force between the top and bottom plates, thus, the horizontal load connection design must be iterated. Suggestions to tackle this are explored in section 2.4.

2.4 Further Steps

The safety factor can be improved by either increasing the bolt preload, which can be done by:

- replacing the existing M16 with larger screws (M20 etc.) or
- adding an additional screw;

or by implementing a pin or c-shape (Figure 16) support to the bottom plate, both of which would take some of the shear force.

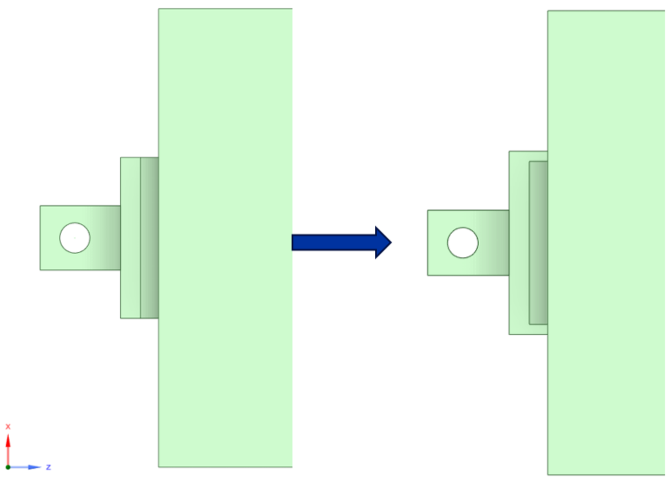

Figure 16: C-shape support for the horizontal lifting component.

However, using a larger screw, which is a hard element, in the relatively soft S235J plate might prevent the expected benefit of increasing the preload due to a possible plastic deformation.

2.5 Conclusion

Overall, the current vertical lifting components comply with the load lifting (EN 13155:2020) and steel joint (EN 1993-1-8) standards. However, the horizontal lifting bottom component design must be improved to increase the safety factors, which can be done by either tackling the pre-load of the screws or the shear force between the two plates.

References

[1] M. Krupa, D. Bett, I. Degl'Innocenti, D. Gudkov, and G. Schneider, "HL-LHC BPM System Development Status," in *Proceedings of the 11th International Beam Instrumentation Conference (IBIC 2022)*. Cracow, Poland: JACoW Publishing, September 2022, pp. 408–412.

[2] P. Forck, P. Kowina, and D. Liakin, "Beam position monitors," in *CAS - CERN Accelerator School: Course on Beam Diagnostics*. Dourdan, France: CERN, 2009.

[3] Hamilton Precision Metals, "Stainless Steel 304L," https://www.hpmetals.com/products/materials/stainless-steel-strip-foil/ss-304l?, Accessed: 2024-08-15.

[4] Sidermariotti, "Data Sheet AISI 304L," https://www.sidermariotti.com/stainless-steel/austenitic/304l.html, 2024, Acessed: 2024-08-15.

[5] O. S. Sandeep and B. Kuriachen, "Influence of build direction and heat treatment on the microstructure and tensile characteristics of cold metal transfer based wire arc additive manufactured SS 304L," *CIRP Journal of Manufacturing Science and Technology*, vol. 47, pp. 59–70, 2023.

[6] Thyssenkrupp Materials, "Stainless Steel 304L," https://www.thyssenkrupp-materials.co.uk/stainless-steel-304l-14307.html, n.d., Accessed: 2024-08-24.

[7] A. Unterstell, "Datasheet," https://www.metalcor.de/en/datenblatt/6/, n.d., Accessed: 2024-09-24.

[8] D. Tommasini, "The PS Booster, PS and SPS Magnets for the Next 25 Years," CERN, Tech. Rep. CERN-TE-Note-2010-003, 2010. [Online]. Available: https://cds.cern.ch/record/1233948/files/CERN%20TE%20Note%202010-003.pdf#:~:text=This%20note%20provides%20information%20and%20analysis

[9] European Committee for Standardization, "Crane - Safety - Non-Fixed Load Lifting Attachments," December 2020, accessed: 2024-15-09. [Online]. Available: https://doi.org/10.3403/30360262

[10] European Committee for Standardization (CEN), "Eurocode 3: Design of Steel Structures - Part 1-8: Design of Joints," 2005, [Authority: The European Union per Regulation 305/2011, Directive 98/34/EC, Directive 2004/18/EC].